

# 3D-GOI: 3D GAN Omni-Inversion for Multifaceted and Multi-object Editing

Haoran Li<sup>1</sup>, Long Ma<sup>1</sup>, Yanbin Hao<sup>1</sup>, Yong Liao<sup>1</sup>, Lechao Cheng<sup>2</sup>, Pengyuan Zhou<sup>\*1</sup>

<sup>1</sup>University of Science and Technology of China, <sup>2</sup>Zhejiang Lab

{lhr123, longm, yliao, pyzhou}@mail.ustc.edu.cn

haoyanbin@hotmail.com, chenglc@zhejianglab.com

## Abstract

*The current GAN inversion methods typically can only edit the appearance and shape of a single object and background while overlooking spatial information. In this work, we propose a 3D editing framework, 3D-GOI to enable multifaceted editing of affine information (scale, translation, and rotation) on multiple objects. 3D-GOI realizes the complex editing function by inverting the abundance of attribute codes (object shape/appearance/scale/rotation/translation, background shape/appearance, and camera pose) controlled by GIRAFFE, a renowned 3D GAN. Accurately inverting all the codes is challenging, 3D-GOI solves this challenge following three main steps. First, we segment the objects and the background in a multi-object image. Second, we use a custom Neural Inversion Encoder to obtain coarse codes of each object. Finally, we use a round-robin optimization algorithm to get precise codes to reconstruct the image. To the best of our knowledge, 3D-GOI is the first framework to enable multifaceted editing on multiple objects. Both qualitative and quantitative experiments demonstrate that 3D-GOI holds immense potential for flexible, multifaceted editing in complex multi-object scenes.*

## 1. Introduction

With the development of generative 3D models, researchers are becoming increasingly interested in generating and editing 3D objects to enhance the automation of multi-object scene generation. However, most existing works are limited to generating and editing a single object, such as 3D face generation [4] and synthesis of facial viewpoints [24]. There are few methods for generating multi-object 3D scenes while editing such scenes remains unexplored. In this paper, we propose 3D-GOI to edit images containing multiple objects with complex spatial geometric relationships. 3D-GOI not only can change the appearance and shape of each object and the background, but also can edit the spatial position of each object and the camera pose of the image as shown by Figure 1.

Existing 3D multi-object scenes generation methods can be mainly classified into two categories: those based on Generative Adversarial Networks (GANs) [5] and those based on diffusion models [8], besides a few based on VAE or Transformer [2, 22]. GAN-based methods, primarily represented by GIRAFFE [17] and its derivatives, depict complex scene images as results of multiple foreground objects, controlled by shape and appearance, being subjected to affine transformations (scaling, translation, and rotation), and rendered together with a background, which is also controlled by shape and appearance, from a specific camera viewpoint. On the other hand, diffusion-based methods [14] perceive scene images as results of multiple latent NeRF [15], which can be represented as 3D models, undergoing affine transformations, optimized with SDS [18], and then rendered from a specific camera viewpoint. Both categories inherently represent scenes as combinations of multiple codes. To realize editing based on these generative methods, it's imperative to invert the complex multi-object scene images to retrieve their representative codes. After modifying these codes, regeneration can achieve diversified editing of complex images. However, most of the current inversion methods study the inversion of a single code based on its generation method, yet the inversion of multiple codes in complex multi-object scenes is largely overlooked. Each multi-object image is the entangled result of multiple codes, to invert all codes from an image requires precise disentangling of the codes which is extremely difficult. Moreover, the prevailing inversion algorithms (for single code) primarily employ optimization approaches. Attempting to optimize all codes simultaneously often leads to chaotic optimization directions, preventing accurate inversion outcomes.

In the face of these challenges, we propose 3D-GOI a framework capable of addressing the inversion of multiple codes, aiming to achieve a comprehensive inversion of multi-object images. Given the current open-source code availability for 3D multi-object scene generation methods, we have chosen GIRAFFE [17] as our generative model. In theory, our framework can be applied to other generative

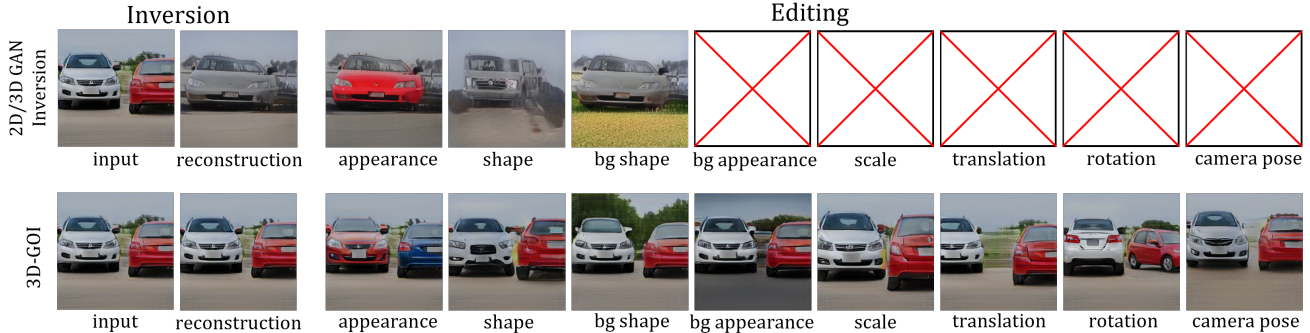


Figure 1. The first row shows the editing results of traditional 2D/3D GAN inversion methods on multi-object images. The second row showcases our proposed 3D-GOI, which can perform multifaceted editing on complex images with multiple objects. 'bg' stands for background. The red crosses in the upper right figures indicate features that cannot be edited with current 2D/3D GAN inversion methods.

approaches as well.

We address this challenge as follows. First, we categorize different codes based on object attributes, background attributes, and pose attributes. Through qualitative verification, we found that segmentation methods can roughly separate the codes pertaining to different objects. For example, the codes controlling an object’s shape, appearance, scale, translation, and rotation predominantly relate to the object itself. So during the inversion process, we only use the segmented image of this object, which can reduce the impact of the background and other objects on its attribute codes.

Second, we get the codes corresponding to attributes from the segmented image. Inspired by the Neural Rendering Block in GIRAFFE, we design a custom Neural Inversion Encoder network to coarsely disentangle and estimate the values of various attribute codes.

Finally, we obtain precise values for each code through optimization. We found that optimizing all codes simultaneously tends to get stuck in local minima. Therefore, we propose a round-robin optimization algorithm that employs a ranking function to determine the optimization order for different codes. The algorithm enables a stable and efficient optimization process for accurate image reconstruction. Our contributions can be summarized as follows.

- To our knowledge, we are the first to propose a multi-code inversion framework in generative models, achieving multifaceted editing of multi-object images.
- We introduce a three-stage inversion process: 1) separate the attribute codes of different objects via the segmentation method; 2) obtain coarse codes of the image using a custom Neural Inversion Encoder; 3) optimize the reconstruction using a round-robin optimization strategy.
- Our method outperforms state-of-the-art methods on multiple datasets on both 3D and 2D tasks.

Due to space limitations, we have included discussions on related work, detailed preliminary studies, implementation details, and additional experiments in the Supplementary Material.

## 2. Preliminary

GIRAFFE [17] represents individual objects as a combination of feature field and volume density. Through scene compositions, the feature fields of multiple objects and the background are combined. Finally, the combined feature field is rendered into an image using volume rendering and neural rendering. The details are described as follows.

For a coordinate  $\mathbf{x}$  and a viewing direction  $\mathbf{d}$  in scene space, the affine transformation  $T(s, t, r)$  ( $s$  represents scale,  $t$  represents translation,  $r$  represents rotation) is used to transform them back into the object space of each individual object. Following the implicit shape representations used in Neural Radiance Fields (NeRF) [16], a multi-layer perceptron (MLP)  $h_\theta$  is used to map the transformed  $\mathbf{x}$  and  $\mathbf{d}$ , along with the shape-controlling code  $z_s$  and appearance-controlling code  $z_a$ , to the feature field  $\mathbf{f}$  and volume density  $\sigma$  as expressed below:

$$(T(s, t, r; \mathbf{x}), T(s, t, r; \mathbf{d})), z_s, z_a \xrightarrow{h_\theta} (\sigma, \mathbf{f}). \quad (1)$$

Then, GIRAFFE defines a Scene Composite Operator: at a given coordinate  $\mathbf{x}$  and viewing direction  $\mathbf{d}$ , the overall density is the sum of the individual densities (including the background). The overall feature field is represented as the density-weighted average of the feature field of each object, as expressed below:

$$C(\mathbf{x}, \mathbf{d}) = (\sigma, \frac{1}{\sigma} \sum_{i=1}^N \sigma_i \mathbf{f}_i), \text{ where } \sigma = \sum_{i=1}^N \sigma_i, \quad (2)$$

where  $N$  denotes the background plus  $(N-1)$  objects.

The rendering phase is divided into two stages. Similar to volume rendering in NeRF [16], given a pixel point, the rendering formula is used to calculate the feature field of this pixel point from the feature fields and the volume density of all sample points in the direction of a camera ray direction. After calculating for all pixel points, a feature map is obtained. Neural rendering (Upsampling) is then applied

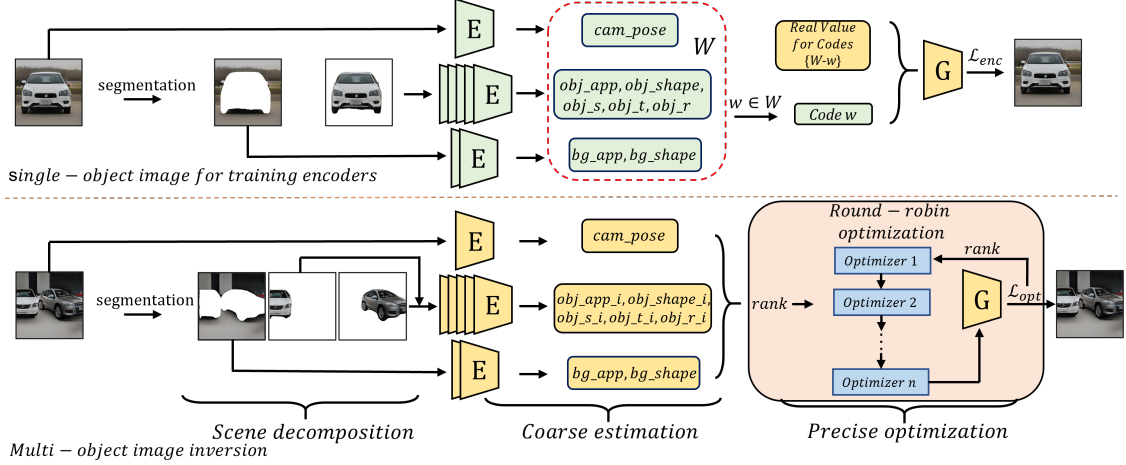


Figure 2. The overall framework of 3D-GOI. As shown in the upper half, the encoders are trained on single-object scenes, each time using  $L_{enc}$  to predict one  $w, w \in W$ , while other codes use real values. The lower half depicts the inversion process for the multi-object scene. We first decompose objects and background from the scene, then use the trained encoder to extract coarse codes, and finally use the round-robin optimization algorithm to obtain precise codes. The green blocks indicate required training and the yellow blocks indicate fixed parameters.

to get the rendered image. Please refer to the Appendix ?? for the detailed preliminary and formulas.

### 3. 3D-GOI

In this section, we present the problem definition of 3D-GOI and our three-step inversion method: scene decomposition, coarse estimation, and precise optimization, as depicted in Figure 2.

#### 3.1. Problem Definition

The problem we target is similar to the general definition of GAN inversion, with the difference being that we need to invert many more codes than existing methods(1 or 2) as shown in Figure 3. The parameter  $w$  in GIRAFFE, which controls the generation of images, can be divided into three categories: object attributes, background attributes, and pose attributes. We use the prefix *obj* to denote object attributes, *bg* for background attributes, and *camera\_pose* for pose attributes. As such,  $w$  can be denoted as follows:

$$W = \{obj\_shape_i, obj\_app_i, obj\_s_i, obj\_t_i, obj\_r_i, bg\_shape, bg\_app, cam\_pose\} \quad i = 1, \dots, n, \quad (3)$$

where *obj\_shape* is the object shape latent code, *obj\_app* is the object appearance latent code, *obj\_s* is the object scale code, *obj\_t* is the object translation code, *obj\_r* is the object rotation code, *bg\_shape* is the background shape latent code, *bg\_app* is the background appearance latent code and *cam\_pose* is the camera pose matrix.  $n$  denotes the  $n$  objects. Then, the reconstruction part of the inversion task can be expressed as:

$$W^* = \arg \min_W \mathcal{L}(G(W, \theta), I), \quad (4)$$

where  $G$  denotes the generator,  $\theta$  denotes the parameters of the generator,  $I$  is the input image, and  $\mathcal{L}$  is the loss function measuring the difference between the generated and input image. According to Equation 3, we need to invert a total of  $(5n + 3)$  codes. Then, we are able to replace or interpolate any inverted code(s) to achieve multifaceted editing of multiple objects.

#### 3.2. Scene Decomposition

As mentioned in previous sections, the GIRAFFE generator differs from typical GAN generators in that a large number of codes are involved in generating images, and not a single code controls the generation of all parts of the image. Therefore, it is challenging to transform all codes using just one encoder or optimizer as in typical GAN Inversion methods. A human can easily distinguish each object and some of its features (appearance, shape) from an image, but a machine algorithm requires a large number of high-precision annotated samples to understand what code is expressed at what position in the image.

A straightforward idea is that in images with multiple objects, the attribute codes of an object will map to the corresponding position of the object in the image. For example, translation (*obj\_t*) and rotation (*obj\_r*) codes control the relative position of an object in the scene, scaling (*obj\_s*) and shape (*obj\_shape*) codes determine the contour and shape of the object, and appearance (*obj\_app*) codes control the appearance representation at the position of the object. The image obtained from segmentation precisely encompasses these three types of information, allowing us to invert it and obtain the five attribute codes for the corresponding object. Similarly, for the codes (*bg\_app, bg\_shape*) that generate the background, we can invert them using the segmented

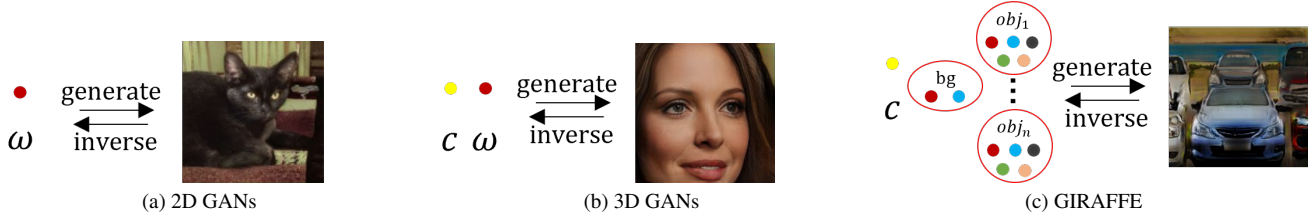


Figure 3. Figure (a) represents the typical 2D GANs and 2D GAN Inversion methods, where one latent encoding corresponds to one image. Figure (b) represents the typical 3D GANs and 3D GAN Inversion methods, which usually have an additional camera pose code  $c$ . Both of these methods can only generate and invert single objects. Figure (c) represents GIRAFFE, which can generate complex multi-object scenes. Each object is controlled by appearance, shape, scale, translation, and rotation, while the background is controlled by appearance and shape. Similarly,  $c$  controls the camera pose, so there are generally  $(5n+3)$  codes, far more than the number of codes in a typical GAN. Therefore, inverting it is a very challenging task. 'bg' means background and 'obj' means object.

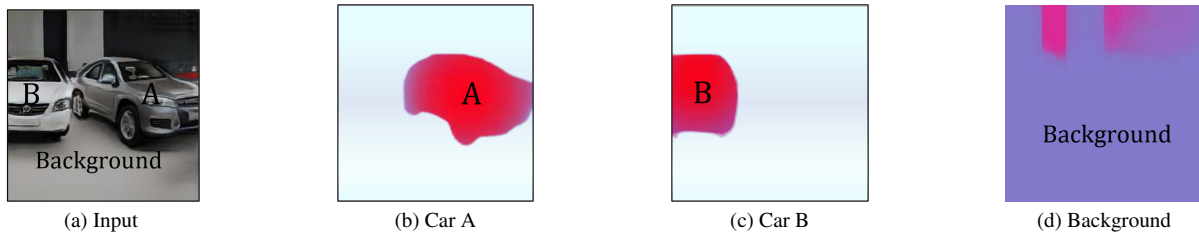


Figure 4. Scene decomposition. (a) is the input image. (b) is the feature weight map of car A, where the redder regions indicate a higher opacity for car A and the bluer regions indicate lower opacity. Similarly, (c) is the feature weight map of car B, and (d) represents the feature weight map of the background. By integrating these maps, it becomes apparent that the region corresponding to car A predominantly consists of the feature representation of car A and likewise for car B. And the visible area of the background solely contains the feature representation of the background.

image of the background. Note that obtaining *cam\_pose* requires information from the entire rendered image.

We can qualitatively validate this idea. In Equation 1, we can see that an object's five attribute codes are mapped to the object's feature field and volume density through  $h_\theta$ . As inferred from Equation 2, the scene's feature field is synthesized by weighting the feature fields of each object by density. Therefore, the reason we see an object appear at its position in the scene is due to its feature field having a high-density weight at the corresponding location. Figure 4 displays the density of different objects at different positions during GIRAFFE's feature field composition process. The redder the color, the higher the density, while the bluer the color, the lower the density. As we discussed, car A exhibits a high-density value within its own area and near-zero density elsewhere - a similar pattern is seen with car B. The background, however, presents a non-uniform density distribution across the entire scene. we can consider that both car A and car B and the background mainly manifest their feature fields within their visible areas. Hence, we apply a straightforward segmentation method to separate each object's feature field and get the codes.

Segmenting each object also has an important advantage: it allows our encoder to pay more attention to each input object or background. As such, we can train the encoder on single-object scenes and then generalize it to multi-object scenes instead of directly training in multi-object scenes that involve more codes, to reduce computation cost.

### 3.3. Coarse Estimation

The previous segmentation step roughly disentangles the codes. Unlike typical encoder-based methods, it's difficult to predict all codes using just one encoder. Therefore, we assign an encoder to each code, allowing each encoder to focus solely on predicting one code. Hence, we need a total of eight encoders. As shown in Figure 2, we input the object segmentation for the object attribute codes (*obj\_shape*, *obj\_app*, *obj\_s*, *obj\_t*, *obj\_r*), the background segmentation for the background attribute codes (*bg\_shape*, *bg\_app*), and the original image for pose attribute code (*cam\_pose*). Different objects share the same encoder for the same attribute code.

We allocate an encoder called Neural Inversion Encoder with a similar structure to each code. Neural Inversion Encoder consists of three parts as Figure 5(b) shows. The first part employs a standard feature pyramid over a ResNet [6] backbone like in pSp [19] to extract the image features. The second part, in which we designed a structure opposite to GIRAFFE's Neural rendering Block based on its architecture as Figure 5(a) shows, downsamples the images layer by layer using a Convolutional Neural Network (CNN) and then uses skip connections [6] to combine the layers, yielding a one-dimensional feature. The third layer employs an MLP structure to acquire the corresponding dimension of different codes. Please refer to the Supplementary Materials 3.1 for the detailed structure of our Neural Inversion Encoder.

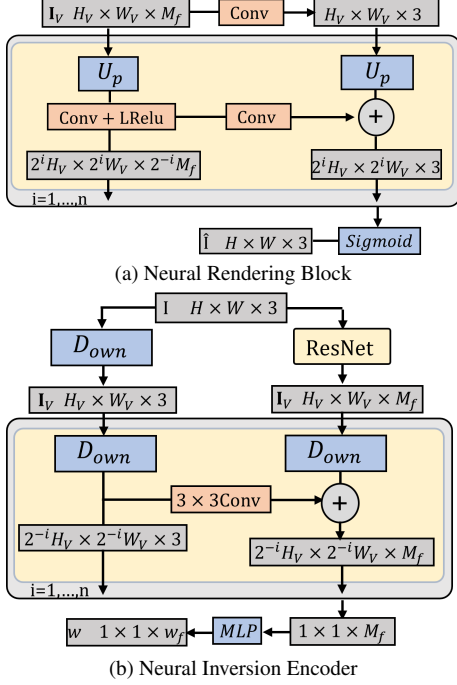


Figure 5. The design of Neural Inversion Encoder. (a) represents the Neural Rendering Block in GIRAFFE [17], which is an upsampling process to generate image  $\hat{I}$ . In contrast, (b) illustrates the Neural Inversion Encoder that opposes it, which is a downsampling process.  $I$  is the input image,  $H, W$  are image height and width.  $I_v$  denotes the heatmap of the image,  $H_v, W_v$  and  $M_f$  are the dimensions of  $I_v$ ,  $w$  is the code to be predicted, and  $w_f$  is the dimension of  $w$ . Up means upsampling and Down means downsampling.

Training multiple encoders simultaneously is difficult to converge due to the large number of training parameters. Hence, we use the dataset generated by GIRAFFE for training to retain the true values of each code and train an encoder for one code at a time, to keep the other codes at their true values. Such a strategy greatly ensures smooth training.

During encoder training, we use the Mean Squared Error (MSE) loss, perceptual loss (LPIPS) [25], and identity loss (ID) [7] between the reconstructed image and the original image, to be consistent with most 2D and 3D GAN inversion training methodologies. When training the affine codes (scale  $s$ , translation  $t$ , rotation  $r$ ), we find that different combinations of values produce very similar images, e.g., moving an object forward and increasing its scale yield similar results. However, the encoder can only predict one value at a time, hence we add the MSE loss of the predicted  $s, t, r$  values, and their true values, to compel the encoder to predict the true value.

$$\mathcal{L}_{enc} = \lambda_1 L_2 + \lambda_2 L_{lpi\text{ps}} + \lambda_3 L_{id}, \quad (5)$$

where  $\lambda_i, i = 1, 2, 3$  represent the ratio coefficient between various losses. When training  $obj\_s, obj\_t, obj\_r$  code, the  $L_2$  loss includes the MSE loss between the real values of

---

### Algorithm 1: Round-robin Optimization

---

**Data:** all codes  $w \in W$  predicted by encoders, fixed GIRAFFE generator  $G$ , input image  $I$ ;

- 1 Initialize  $lr\_w = 10^{-3}, w \in W$ ;
- 2 **while** any  $lr\_w > 10^{-5}$  **do**
- 3     **foreach**  $w \in W$  **do**
- 4         Sample  $\delta w$ ;
- 5         Compute  $\delta \mathcal{L}(w)$  using Eq. 6;
- 6     **end**
- 7     Compute  $rank\_list$  using Eq. 7;
- 8     **foreach**  $w \in rank\_list$  and  $lr\_w > 10^{-5}$  **do**
- 9         Optimization  $w$  with  $\mathcal{L}_{opt}$  in Eq. 8 of  $I$  and  $G(W; \theta)$ ;
- 10         **if** the  $\mathcal{L}_{opt}$  ceases to decrease for five consecutive iterations **then**
- 11              $lr\_w = lr\_w / 2$ ;
- 12         **end**
- 13     **end**
- 14 **end**

---

$obj\_s, obj\_t, obj\_r$  and their predicted values.

### 3.4. Precise Optimization

Next, we optimize the coarse codes predicted by the encoder. Through experiments, we have found that using a single optimizer to simultaneously optimize all latent codes tends to converge to local minima. To circumvent this, we employ multiple optimizers, each handling a single code as in the coarse estimation. The optimization order plays a crucial role in the overall outcome due to the variance of the disparity between the predicted and actual values across different encoders, and the different impact of code changes on the image, e.g., changes to  $bg\_shape$  and  $bg\_app$  codes controlling background generation mostly would have a larger impact on overall pixel values. Prioritizing the optimization of codes with significant disparity and a high potential for changing pixel values tends to yield superior results in our empirical experiments. Hence, we propose an automated round-robin optimization algorithm (Algorithm 1) to sequentially optimize each code based on the image reconstructed in each round.

Algorithm 1 aims to add multiple minor disturbances to each code, and calculate the loss between the images reconstructed before and after the disturbance and the original image. A loss increase indicates that the current code value is relatively accurate, hence its optimization order can be put later. A loss decrease indicates that the current code value is inaccurate and thus should be prioritized. For multiple codes that demand prioritized optimization, we compute their priorities using the partial derivatives of the loss variation and perturbation. We do not use backpropagation au-

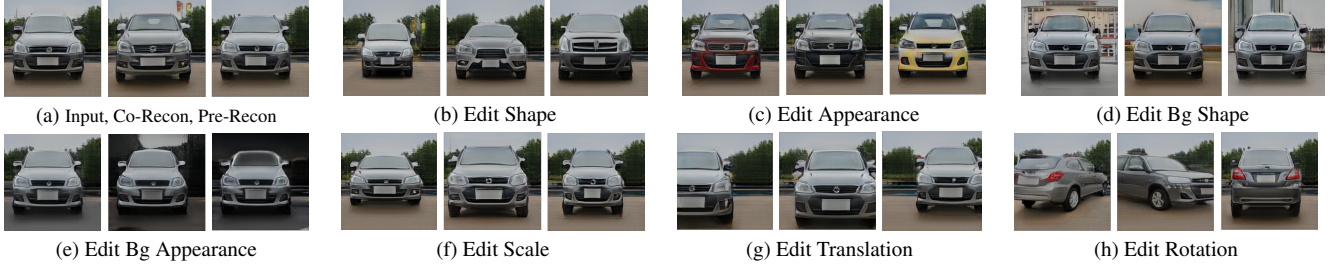


Figure 6. Single-object editing on *G-CompCars* dataset. Co-Recon: coarse reconstruction. Pre-Recon: precise reconstruction.

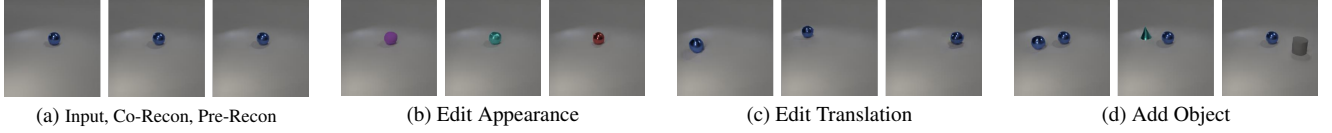


Figure 7. Single-object editing on *Clevr* dataset.

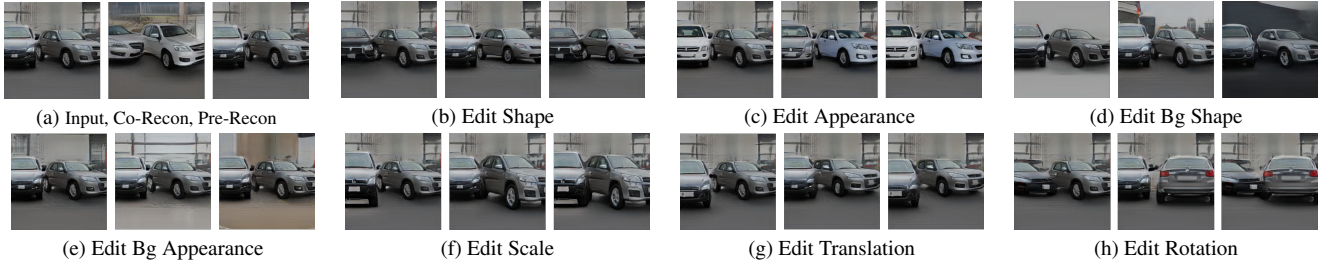


Figure 8. Multi-object editing on *G-CompCars* dataset.



Figure 9. Multi-object editing on *Clevr* dataset.

tomatic differentiation here to ensure the current code value remains unchanged.

$$\delta\mathcal{L}(w) = \mathcal{L}(G(W - \{w\}, w + \delta w, \theta), I) - \mathcal{L}(G(W, \theta), I), \quad (6)$$

$$rank\_list = F_{rank}(\delta\mathcal{L}(w), \frac{\delta\mathcal{L}(w)}{\delta w}), \quad (7)$$

where  $w \in W$  is one of the codes and  $\delta w$  represents the minor disturbance of  $w$ . For the rotation angle  $r$ , we have found that adding a depth loss can accelerate its optimization. Therefore, the loss  $\mathcal{L}$  during the optimization stage can be expressed as:

$$\mathcal{L}_{opt} = \lambda_1 L_2 + \lambda_2 L_{lips} + \lambda_3 L_{id} + \lambda_4 L_{deep}. \quad (8)$$

This optimization method allows for more precise tuning of the codes for more accurate reconstruction and editing of the images.

## 4. Experiment

**Datasets.** To obtain the true values of the 3D information in GIRAFFE for stable training performance, we use the pre-trained model of GIRAFFE on the CompCars [23] dataset and Clevr [9] dataset to generate training datasets. For testing datasets, we also use GIRAFFE to generate images for multi-car datasets denoted as *G-CompCars* (CompCars is a single car image dataset) and use the original Clevr dataset for multi-geometry dataset (Clevr is a dataset that can be simulated to generate images of multiple geometries). We follow the codes setup in GIRAFFE. For CompCars, we use all the codes from Equation 3. For Clevr, we fixed the rotation, scale, and camera pose codes of the objects. For experiments on facial data, we utilized the FFHQ [11] dataset for training and the CelebA-HQ [10] dataset for testing.

**Baselines.** In the comparative experiments for our Neural Inversion Encoder, we benchmarked encoder-based inversion methods such as e4e [20] and pSp [19], which use the 2D GAN StyleGAN2 [12] as the generator, and

E3DGE [13] and TriplaneNet [3] that employ the 3D GAN EG3D [4] as the generator, on the generator of GIRAFFE. Additionally, we compared our encoder on StyleGAN2 with SOTA inversion methods HyperStyle [1] and HFGI [21] for StyleGAN2.

**Metrics.** We use Mean Squared Error (MSE), perceptual similarity loss (LPIPS) [25], and identity similarity (ID) to measure the quality of image reconstruction.

## 4.1. 3D GAN Omni-Inversion

### 4.1.1 Single-object Multifaceted Editing

In Figure 6 and Figure 7, (a) depict the original images, the coarsely reconstructed images produced by the Neural Inversion Encoder, and the precisely reconstructed images obtained via round-robin optimization. As Figure 7 shows, the simple scene structure of the Clevr dataset allows us to achieve remarkably accurate results using only the encoder (Co-Recon). However, for car images in Figure 6, predicting precise codes using the encoder only becomes challenging, necessitating the employment of the round-robin optimization algorithm to refine the code values for precise reconstruction (Pre-Recon). Figure 6 (b)-(h) and Figure 7 (b)-(d) show the editing results for different codes. As noted in Section 3.3, moving an object forward and increasing its scale yield similar results. Due to space constraints, please refer to the Supplementary Material 4.1 for more results like camera pose and shape editing.

### 4.1.2 Multi-object Multifaceted Editing

We notice that the prediction for some object parameters (*obj\_shape*, *obj\_app*, *obj\_s*, *obj\_t*) are quite accurate. However, the prediction for the background codes deviates significantly. We speculate this is due to the significant differences in segmentation image input to the background encoder between multi-object scenes and single-object scenes. Therefore, background reconstruction requires further optimization. Figure 8 and Figure 9 depict the multifaceted editing outcomes for two cars and multiple Clevr objects, respectively. The images show individual edits of two objects in the left and middle images and collective edits at the right images in Figure 8 (b-c) and (f-h). As demonstrated in Figure 8, the predictive discrepancy between the background and the rotation angle of the car on the left is considerable, requiring adjustments through the round-robin optimization algorithm. As illustrated in Figure 1, 2D/3D GAN inversion methods can not inverse multi-object scenes. More images pertaining to multi-object editing can be found in the Supplementary Material 4.2.

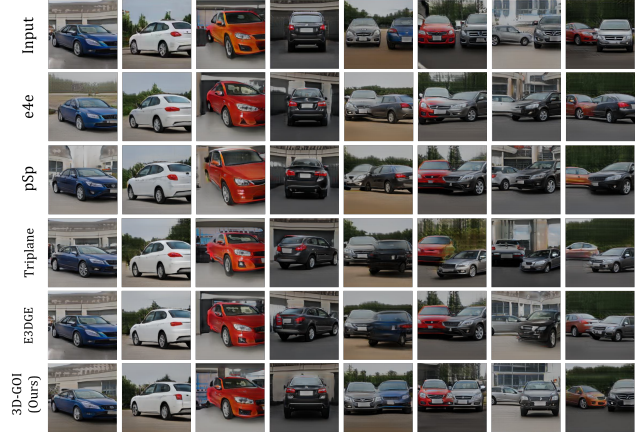


Figure 10. Reconstruction results of different GAN inversion encoders using the generator of GIRAFFE.



Figure 11. Reconstruction results of different GAN inversion encoders using the generator of StyleGAN2.

## 4.2. Comparison Experiment of Neural Inversion Encoder

For fair comparison and to eliminate the impact of the generator on the quality of the inverted image generation, we trained the encoders from the baseline methods by connecting them to the GIRAFFE generator using our Neural Inversion Encoder training approach and compared them with our Neural Inversion Encoder. At the same time, we also connected our encoder to StyleGAN2 and compared it with inversion methods based on StyleGAN2, thereby demonstrating the efficiency of our encoder design. Table 1 quantitatively displays the comparison results on both the GIRAFFE and StyleGAN2 generators. The results show that our Neural Inversion Encoder consistently outperforms baseline methods. Figure 10 shows the performance comparison between our Neural Inversion Encoder and other baseline encoders using the GIRAFFE generator under the same training settings. Evidently, our method achieves the best results in both single-object and multi-object inversion reconstructions. Figure 11 shows the performance com-

Table 1. Reconstruction quality of different GAN inversion encoders using the generator of GIRAFFE and StyleGAN2. ↓ indicates the lower the better and ↑ indicates the higher the better.

Method	GIRAFFE for Generator			StyleGAN2 for Generator		
	MSE ↓	LPIPS ↓	ID ↑	MSE ↓	LPIPS ↓	ID ↑
e4e [20]	0.031	0.306	0.867	0.052	0.200	0.502
pSp [19]	0.031	0.301	0.877	0.034	0.172	0.561
HyperStyle [1]	-	-	-	0.019	0.091	0.766
HFGI [21]	-	-	-	0.023	0.124	0.705
TriplaneNet [3]	0.029	0.296	0.870	-	-	-
E3DGE [13]	0.031	0.299	0.881	-	-	-
3D-GOI(Ours)	<b>0.024</b>	<b>0.262</b>	<b>0.897</b>	<b>0.017</b>	<b>0.098</b>	<b>0.769</b>

Table 2. Ablation Study of the Neural Inversion Encoder.

Method	MSE ↓	LPIPS ↓	ID ↑
w/o NIB	0.023	0.288	0.856
w/o MLP	0.015	0.183	0.878
3D-GOI	<b>0.010</b>	<b>0.141</b>	<b>0.906</b>

Table 3. The quantitative metrics of ablation study of the Round-robin Optimization algorithm.

Method	MSE ↓	LPIPS ↓	ID ↑
Order1	0.016	0.184	0.923
Order2	0.019	0.229	0.913
Order3	0.019	0.221	0.911
3D-GOI	<b>0.008</b>	<b>0.128</b>	<b>0.938</b>

parison between our method and the baselines using StyleGAN2 as the generator. Our method clearly outperforms the baselines in the inversion of details such as hair and teeth.

As such, we can conclude that our Neural Inversion Encoder performs excellent inversion on different 2D StyleGAN2 and 3D GIRAFFE, both qualitatively and quantitatively.

### 4.3. Ablation Study

We conducted ablation experiments separately for the proposed Neural Inversion Encoder and the Round-robin Optimization algorithm.

Table 2 displays the average ablation results of the Neural Inversion Encoder on various attribute codes, where NIB refers to Neural Inversion Block (the second part of the encoder) and MLP is the final part of the encoder. The results clearly show that our encoder structure is extremely effective and can predict code values more accurately. Please find the complete results in the Supplementary Material 4.4.

For the Round-robin optimization algorithm, we compared it with three fixed optimization order algorithms on both single-object and multi-object scenarios. The three fixed sequences are as follows:

$$Order1 : bg\_shape, bg\_app, \{obj\_r_i, obj\_t_i, obj\_s_i\}_{i=1}^N,$$

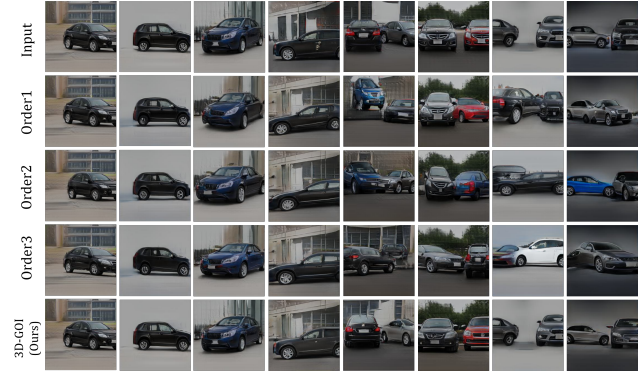


Figure 12. The figure of ablation study of the round-robin Optimization algorithm.

$$\{obj\_shape_i, obj\_app_i\}_{i=1}^N, camera\_pose$$

$$Order2 : \{obj\_r_i, obj\_t_i, obj\_s_i\}_{i=1}^N, \{obj\_shape_i, obj\_app_i\}_{i=1}^N, bg\_shape, bg\_app, camera\_pose$$

$$Order3 : camera\_pose, \{obj\_shape_i, obj\_app_i\}_{i=1}^N, \{obj\_r_i, obj\_t_i, obj\_s_i\}_{i=1}^N, bg\_shape, bg\_app$$

$\{\}_{i=1}^N$  indicates that the elements inside  $\{\}$  are arranged in sequence from 1 to N. There are many possible sequence combinations, and here we chose **the three with the best results** for demonstration. Table 3 and Figure 12 are the quantitative and qualitative comparison of the four methods. As shown, our method achieves the best results on all metrics, demonstrating the effectiveness of our Round-robin optimization algorithm. As mentioned in 3.4, optimizing features like the image background first can enhance the optimization results. Hence, Order1 performs much better than Order2 and Order3.

## 5. Conclusion

This paper introduces a 3D GAN inversion method, 3D-GOI, that enables multifaceted editing of scenes containing multiple objects. By using a segmentation approach to separate objects and background, then carrying out a coarse estimation followed by a precise optimization, 3D-GOI can accurately obtain the codes of the image. These codes are

then used for multifaceted editing. To the best of our knowledge, 3D-GOI is the first method to attempt multi-object & multifaceted editing. We anticipate that 3D-GOI holds immense potential for future applications in fields such as VR/AR, and the Metaverse.

## References

- [1] Yuval Alaluf, Omer Tov, Ron Mokady, Rinon Gal, and Amit Bermano. Hyperstyle: Stylegan inversion with hypernetworks for real image editing. In *Proceedings of the IEEE/CVF conference on computer vision and pattern recognition*, pages 18511–18521, 2022. [7](#), [8](#)
- [2] Dor Arad Hudson and Larry Zitnick. Compositional transformers for scene generation. *Advances in Neural Information Processing Systems*, 34:9506–9520, 2021. [1](#)
- [3] Ananta R Bhattarai, Matthias Nießner, and Artem Sevastopolsky. Triplanenet: An encoder for eg3d inversion. *arXiv preprint arXiv:2303.13497*, 2023. [7](#), [8](#)
- [4] Eric R Chan, Connor Z Lin, Matthew A Chan, Koki Nagano, Boxiao Pan, Shalini De Mello, Orazio Gallo, Leonidas J Guibas, Jonathan Tremblay, Sameh Khamis, et al. Efficient geometry-aware 3d generative adversarial networks. In *Proceedings of the IEEE/CVF Conference on Computer Vision and Pattern Recognition*, pages 16123–16133, 2022. [1](#), [7](#)
- [5] Ian Goodfellow, Jean Pouget-Abadie, Mehdi Mirza, Bing Xu, David Warde-Farley, Sherjil Ozair, Aaron Courville, and Yoshua Bengio. Generative adversarial networks. *Communications of the ACM*, 63(11):139–144, 2020. [1](#)
- [6] Kaiming He, Xiangyu Zhang, Shaoqing Ren, and Jian Sun. Deep residual learning for image recognition. In *Proceedings of the IEEE conference on computer vision and pattern recognition*, pages 770–778, 2016. [4](#)
- [7] Kaiming He, Haoqi Fan, Yuxin Wu, Saining Xie, and Ross Girshick. Momentum contrast for unsupervised visual representation learning. In *Proceedings of the IEEE/CVF conference on computer vision and pattern recognition*, pages 9729–9738, 2020. [5](#)
- [8] Jonathan Ho, Ajay Jain, and Pieter Abbeel. Denoising diffusion probabilistic models. *Advances in neural information processing systems*, 33:6840–6851, 2020. [1](#)
- [9] Justin Johnson, Bharath Hariharan, Laurens Van Der Maaten, Li Fei-Fei, C Lawrence Zitnick, and Ross Girshick. Clevr: A diagnostic dataset for compositional language and elementary visual reasoning. In *Proceedings of the IEEE conference on computer vision and pattern recognition*, pages 2901–2910, 2017. [6](#)
- [10] Tero Karras, Timo Aila, Samuli Laine, and Jaakko Lehtinen. Progressive growing of gans for improved quality, stability, and variation. *arXiv preprint arXiv:1710.10196*, 2017. [6](#)
- [11] Tero Karras, Samuli Laine, and Timo Aila. A style-based generator architecture for generative adversarial networks. In *Proceedings of the IEEE/CVF conference on computer vision and pattern recognition*, pages 4401–4410, 2019. [6](#)
- [12] Tero Karras, Samuli Laine, Miika Aittala, Janne Hellsten, Jaakko Lehtinen, and Timo Aila. Analyzing and improving the image quality of stylegan. In *Proceedings of the IEEE/CVF conference on computer vision and pattern recognition*, pages 8110–8119, 2020. [6](#)
- [13] Yushi Lan, Xuyi Meng, Shuai Yang, Chen Change Loy, and Bo Dai. Self-supervised geometry-aware encoder for style-based 3d gan inversion. In *Proceedings of the IEEE/CVF Conference on Computer Vision and Pattern Recognition*, pages 20940–20949, 2023. [7](#), [8](#)
- [14] Yiqi Lin, Haotian Bai, Sijia Li, Haonan Lu, Xiaodong Lin, Hui Xiong, and Lin Wang. Componerf: Text-guided multi-object compositional nerf with editable 3d scene layout. *arXiv preprint arXiv:2303.13843*, 2023. [1](#)
- [15] Gal Metzger, Elad Richardson, Or Patashnik, Raja Giryes, and Daniel Cohen-Or. Latent-nerf for shape-guided generation of 3d shapes and textures. *arXiv preprint arXiv:2211.07600*, 2022. [1](#)
- [16] Ben Mildenhall, Pratul P Srinivasan, Matthew Tancik, Jonathan T Barron, Ravi Ramamoorthi, and Ren Ng. Nerf: Representing scenes as neural radiance fields for view synthesis. *Communications of the ACM*, 65(1):99–106, 2021. [2](#)
- [17] Michael Niemeyer and Andreas Geiger. Giraffe: Representing scenes as compositional generative neural feature fields. In *Proceedings of the IEEE/CVF Conference on Computer Vision and Pattern Recognition*, pages 11453–11464, 2021. [1](#), [2](#), [5](#)
- [18] Ben Poole, Ajay Jain, Jonathan T Barron, and Ben Mildenhall. Dreamfusion: Text-to-3d using 2d diffusion. *arXiv preprint arXiv:2209.14988*, 2022. [1](#)
- [19] Elad Richardson, Yuval Alaluf, Or Patashnik, Yotam Nitzan, Yaniv Azar, Stav Shapiro, and Daniel Cohen-Or. Encoding in style: a stylegan encoder for image-to-image translation. In *Proceedings of the IEEE/CVF conference on computer vision and pattern recognition*, pages 2287–2296, 2021. [4](#), [6](#), [8](#)
- [20] Omer Tov, Yuval Alaluf, Yotam Nitzan, Or Patashnik, and Daniel Cohen-Or. Designing an encoder for stylegan image manipulation. *ACM Transactions on Graphics (TOG)*, 40(4):1–14, 2021. [6](#), [8](#)
- [21] Tengfei Wang, Yong Zhang, Yanbo Fan, Jue Wang, and Qifeng Chen. High-fidelity gan inversion for im-

- age attribute editing. In *Proceedings of the IEEE/CVF Conference on Computer Vision and Pattern Recognition*, pages 11379–11388, 2022. 7, 8
- [22] Haitao Yang, Zaiwei Zhang, Siming Yan, Haibin Huang, Chongyang Ma, Yi Zheng, Chandrajit Bajaj, and Qixing Huang. Scene synthesis via uncertainty-driven attribute synchronization. In *Proceedings of the IEEE/CVF International Conference on Computer Vision*, pages 5630–5640, 2021. 1
- [23] Jiaolong Yang and Hongdong Li. Dense, accurate optical flow estimation with piecewise parametric model. In *Proceedings of the IEEE Conference on Computer Vision and Pattern Recognition*, pages 1019–1027, 2015. 6
- [24] Fei Yin, Yong Zhang, Xuan Wang, Tengfei Wang, Xiaoyu Li, Yuan Gong, Yanbo Fan, Xiaodong Cun, Ying Shan, Cengiz Oztireli, et al. 3d gan inversion with facial symmetry prior. *arXiv preprint arXiv:2211.16927*, 2022. 1
- [25] Richard Zhang, Phillip Isola, Alexei A Efros, Eli Shechtman, and Oliver Wang. The unreasonable effectiveness of deep features as a perceptual metric. In *Proceedings of the IEEE conference on computer vision and pattern recognition*, pages 586–595, 2018. 5, 7